The ‘sticky’ ITCZ: ocean-moderated ITCZ shifts

Brian Green, John Marshall & Jean-Michel Campin

Climate Dynamics
Observational, Theoretical and Computational Research on the Climate System

ISSN 0930-7575

Clim Dyn
DOI 10.1007/s00382-019-04623-5

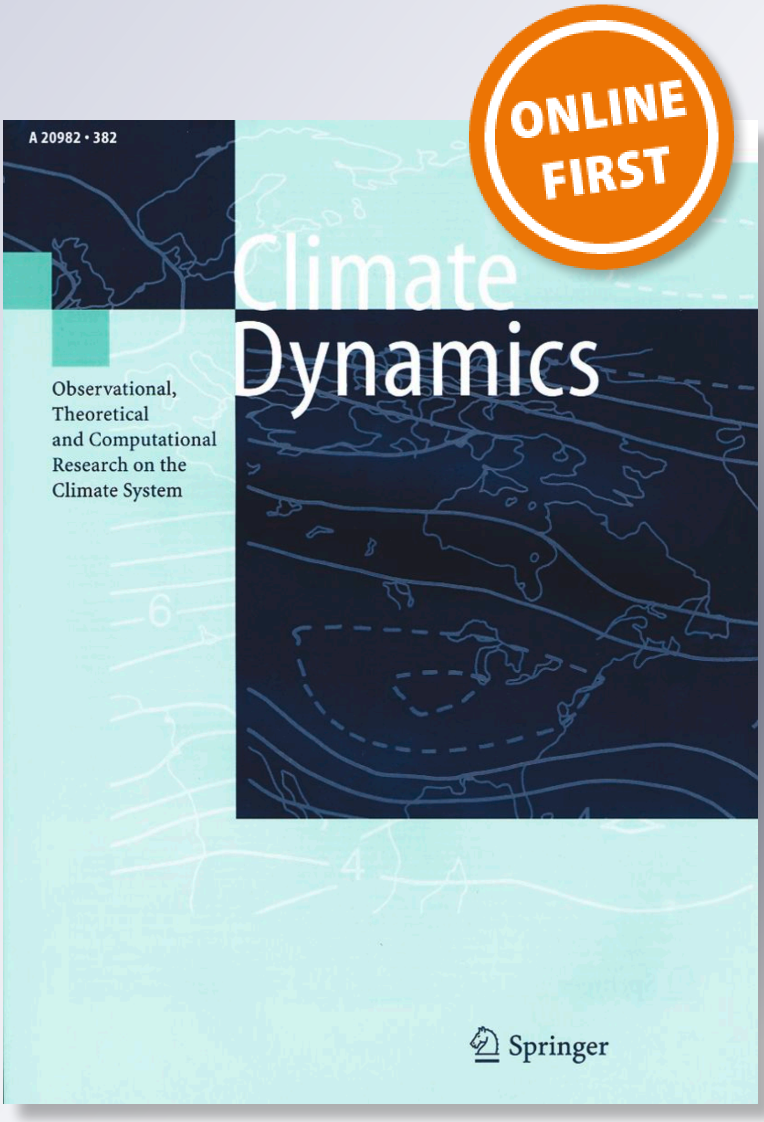

Climate Dynamics
https://doi.org/10.1007/s00382-019-04623-5

The 'sticky' ITCZ: ocean-moderated ITCZ shifts

Brian Green[1,2] · **John Marshall**[1] · **Jean-Michel Campin**[1]

Received: 6 September 2018 / Accepted: 24 November 2018

Abstract

Across a range of simulations with a coupled atmosphere–ocean climate model, shifts in the intertropical convergence zone (ITCZ) are induced by an interhemispheric heating contrast. The response to heating anomalies which are polar amplified are contrasted with those which are largest in the tropics. First, we find that ITCZ shifts are always damped relative to simulations in which the ocean circulation is held fixed, irrespective of the heating distribution, keeping the ITCZ "stuck" to latitudes near the equator. The damping is primarily due to the ocean's anomalous cross-equatorial energy transport associated with the coupling of the trade winds to an oceanic cross-equatorial cell (CEC). Second, we find that the damping effect is strongest when the forcing distribution is polar-amplified, which enhances the gross stability of the CEC and maximizes the efficiency of its cross-equatorial energy transport. Third, we argue that the ocean's energy transport can have secondary impacts on ITCZ shifts through its interaction with climate feedbacks. Finally, we discuss the implications of our study for our understanding of the role of CECs in damping ITCZ shifts and the atmosphere's energy balance.

Keywords Intertropical convergence zone · Trade winds · Hadley cell · Subtropical cell

1 Introduction

Earth's northern hemisphere (NH) is slightly warmer than the southern (SH; Feulner et al. 2013; Marshall et al. 2014; Kang et al. 2015) and its climatic equator is slightly north of the geographical equator. Interestingly, the hemispheric albedos are almost identical to one another and so the solar radiation absorbed in each hemisphere is, to within measurement accuracy, the same: the NH is warm because of cross-equatorial heat transport in the Atlantic sector of a few tenths of a petawatt (10^{15} W; see the discussion in Marshall et al. 2014). But imagine a climate in which the hemispheric albedos were very different, demanding that the coupled atmosphere–ocean system transport large amounts—perhaps many petawatts—of energy across the equator. How would the coupled system achieve this? What would the relative roles of the atmosphere and ocean be in the balancing process? Would the partitioning of the energy transport between atmosphere and ocean be sensitive to whether the heating anomaly were polar- or equatorially-magnified?

Recently, several experiments using comprehensive global climate models (GCMs) forced with interhemispheric heating contrasts have pointed to a role for the tropical ocean circulation in moderating shifts of tropical rainfall patterns and the climatic equator. Known as the intertropical convergence zone, or ITCZ, the tropical rainfall maximum is collocated with the ascending branch of the atmosphere's Hadley cells, shifting with those circulations into the hemisphere heated most strongly by radiation and surface heat fluxes (see the review in Schneider et al. 2014). For example, the tropical precipitation response to SH cooling by brightened clouds (Kay et al. 2016) and NH heating by Arctic sea ice loss (Tomas et al. 2016) is strongly muted in fully coupled atmosphere–ocean simulations compared to runs without an active ocean circulation. In both cases, the ocean circulation's cross-equatorial energy transport is responsible for offsetting a large fraction of the imposed heating contrast. If the ocean's response is decomposed into contributions from each basin, the Pacific Ocean, whose subtropical cells (STCs) are responsible for the majority of the basin's meridional energy transport in the tropics (Ferrari and Ferreira

---

✉ Brian Green
brianmg@uw.edu

[1] Massachusetts Institute of Technology, 77 Massachusetts Ave., Bldg 54, Cambridge, MA 02139, USA

[2] Present Address: Joint Institute for the Study of the Atmosphere and Ocean, University of Washington, 3737 Brooklyn Ave. NE, Seattle, WA 98105, USA

2011), can be the largest contributor to the global response (Hawcroft et al. 2016).

Coupled to the Hadley cells above by the trade winds, the STCs are capable of transporting more energy in the tropics than their atmospheric counterparts (Held 2001; Czaja and Marshall 2006) because they act on the highly stratified tropical ocean. In idealized GCM simulations of a water-covered Earth, experiments with a coupled atmosphere–ocean model (Green and Marshall 2017; hereafter GM17) and an atmospheric model coupled to a stationary slab ocean modified to simulate the STCs (Kang et al. 2018a) have shown that the STCs and their associated CEC act to damp ITCZ shifts. The experiments in GM17 highlighted the basic mechanism behind the damping of ITCZ shifts by the STCs, shown schematically in Fig. 1: the coupling to the atmosphere above by the trade winds generates an anomalous cross-equatorial cell (CEC) whenever the ITCZ shifts off of the equator. The oceanic CEC is capable of transporting more energy across the equator than the Hadley cell above owing to its higher heat capacity and vertical temperature contrast. It is this cross-equatorial energy transport by the CEC, acting to offset the interhemispheric heating contrast, that reduces the amount of energy the Hadley cells must transport across the equator and damps the ITCZ shift. Using a simple energy balance framework, GM17 then showed how the cross-equatorial energy transport by the CEC can damp ITCZ shifts by a factor of four.

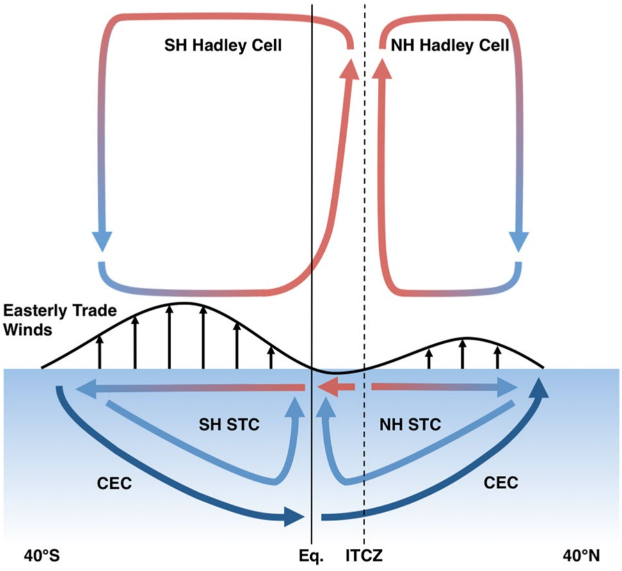

Fig. 1 Schematic of the atmosphere and wind-driven tropical ocean circulations for a northward ITCZ shift. In the atmosphere, the colors of the arrows are meant to represent the moist static energy content of the air circulating in the Hadley cells. In the ocean, the colors represent the temperature of the water masses forming the STCs and the CEC. The equator and the latitude of the ITCZ are indicated with solid and dashed vertical black lines, respectively

Here we further explore the damping of ITCZ shifts through their coupling to the tropical ocean circulation, attempting to induce extreme shifts by varying the magnitude of the interhemispheric heating contrast and its meridional distribution, using the same model as in GM17. We find that cross-equatorial energy transport by the CECs always acts to damp ITCZ shifts but the degree of damping depends on whether the heating profile reaches a maximum at poleward as opposed to equatorward latitudes. To a lesser extent, the degree of damping also depends on the interaction between the ocean's heat transport and radiative feedbacks. Finally, we discuss the implications of our study for ITCZ shifts in the current climate and interpret our results in the context of an energy balance model proposed by Schneider (2017).

2 Model configuration and design of experiments

We use the same model described in GM17, a coupled atmosphere–ocean version of the MITgcm (Marshall et al. 1997a, b, 2004) in configurations with and without an active ocean circulation. Both the atmospheric and oceanic components are run on a cubed-sphere grid with roughly 2.8° horizontal resolution in the tropics (Adcroft et al. 2004). The atmospheric component has 26 pressure levels, moist physics and a gray radiation scheme as in Frierson (2007), and includes a water vapor feedback on the longwave optical thickness as in Byrne and O'Gorman (2013). There are no clouds or shortwave absorption in the atmosphere, making the planetary albedo equal to the surface albedo, which we prescribe to be symmetric about the equator (Fig. 2a). The model is run with a seasonal cycle of insolation for a circular orbit with an obliquity of 23.45°.

The oceanic component of the model is also identical to GM17 and run in a configuration both with and without an active ocean circulation. In the active case, the ocean and its circulation are fully coupled to the atmosphere above; there are 15 vertical levels down to a depth of 3400 m. Two infinitesimally thin ridges, running from the North Pole to 35°S, are spaced 90° longitude apart, creating a small 90°-wide basin, a large 270°-wide basin, and a circumpolar southern ocean. As described in Ferreira et al. (2010), this leads to localization of deep water formation and sinking in the polar latitudes of the small basin, and wind-driven circumpolar upwelling around the south pole, mimicking the global overturning cell of Earth's current climate. In the passive ocean circulation case, referred to as a "slab" ocean, the model has one stationary layer with specified patterns of depth and ocean heat transport convergence that match the annual mean from the fully coupled configuration's control run. Setting up the slab ocean configuration in this way

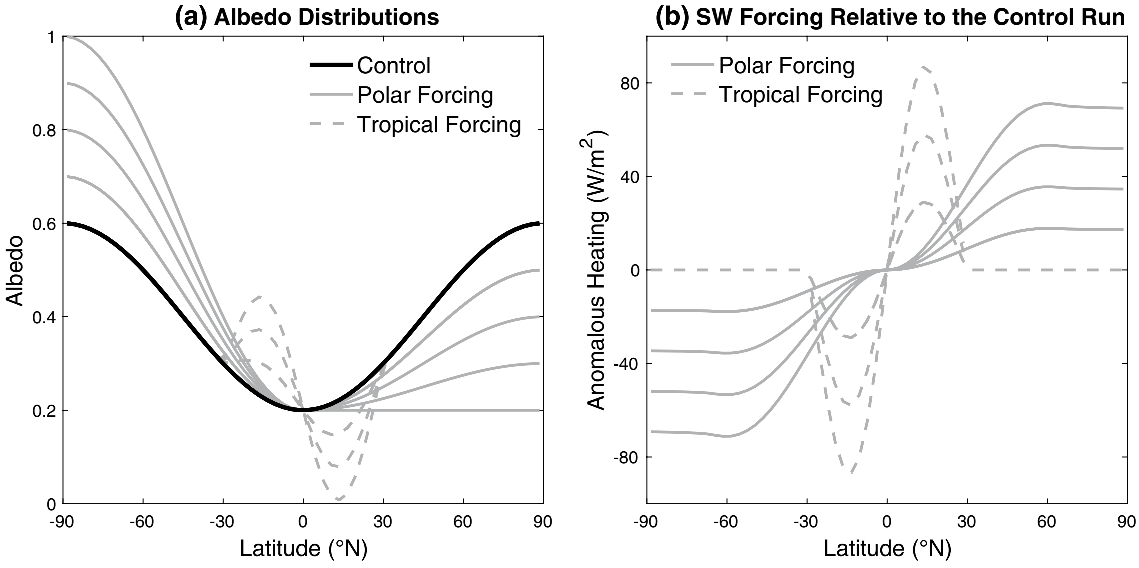

Fig. 2 Distributions of interhemispheric forcing. **a** Surface albedo distributions for the control run (black line), polar forcing cases (solid gray lines), and tropical forcing cases (dashed gray lines). **b** The resulting changes in the net absorbed shortwave radiation in the annual mean

allows us to attribute differences between its response and the fully coupled configuration's response to the forcing described below to the adjustment of the ocean circulation in the fully coupled case.

The control runs of both the slab ocean and fully coupled models are very similar to each other, and identical to those in GM17. Shown in Fig. 3a, the fully coupled control run's annual mean atmospheric circulation is qualitatively similar to the Earth's, with a SH Hadley cell that is stronger (88 Sv) than the NH Hadley cell (71 Sv). Surface easterly trade winds (Fig. 3b) and the STC in the large basin (Fig. 3c) are correspondingly stronger in the SH: 3.0 m s^{-1} and 45 Sv versus 2.7 m s^{-1} and 39 Sv in the NH. Sea surface temperatures (SSTs) are slightly higher in the NH than the SH and peak at 29 °C at the equator; their hemispheric means are 19 and 17 °C, respectively. It should be noted that the model does not form sea ice, resulting in polar SSTs that are below freezing, in which case the model calculates the density of seawater by extrapolating the curves for its equation of state (Jackett and McDougall 1995) below the freezing point. The hemispheric asymmetries of Hadley cell and trade wind strengths, and of SST, are the result of a deep overturning circulation in the small basin that transports heat northward across the equator, as described in Ferreira et al. (2010) and shown in Fig. 3d. This circulation heats the NH, cools the SH, and pushes the Hadley cells and ITCZ slightly north of the equator, similar to the effects of the Atlantic Ocean's deep overturning circulation.

To shift the ITCZ further northward in both the slab and fully coupled models, we rock the hemispherically symmetric albedo distribution of the control run about the equator, reducing its value in the NH at the same rate it is increased in the SH (Fig. 2a). The control albedo distribution α_{ctrl} and changes to it, $\Delta\alpha_{polar}$ for polar-amplified changes and $\Delta\alpha_{tropics}$ for tropics-only changes, are specified as:

$$\alpha_{ctrl} = \frac{1}{5}\left(2x^2 + 1\right) \tag{1a}$$

$$\Delta\alpha_{polar} = -G\frac{x}{|x|}x^2 \tag{1b}$$

$$\Delta\alpha_{tropics} = \begin{cases} -G' \cdot sin(2\pi x), & |x| \leq 0.5 \\ 0, & |x| > ;0.5, \end{cases} \tag{1c}$$

where x is the sine of latitude. The multiplicative constant G specifies the magnitude of the polar-amplified albedo change; for the distributions in Fig. 2a, it ranges from 0.1 to 0.4. In the most extreme case, $G = 0.4$, the NH albedo is a constant 0.2 and the SH albedo increases from 0.2 at the equator to 1.0 at the south pole. For tropics-only changes in albedo, G' is scaled so that when annual mean changes in absorbed shortwave radiation at the surface (Fig. 2b) are averaged over the hemisphere, they match the first three polar-amplified distributions. It has values of 0.07, 0.14, and 0.22, and only three forcing amplitudes are used to prevent the albedo from decreasing below zero. The average heating of the NH is 9.2 W m^{-2} for the lowest-amplitude forcing cases, increasing linearly with G and G'.

The modified albedo distributions are applied instantaneously to control runs of both the fully coupled and

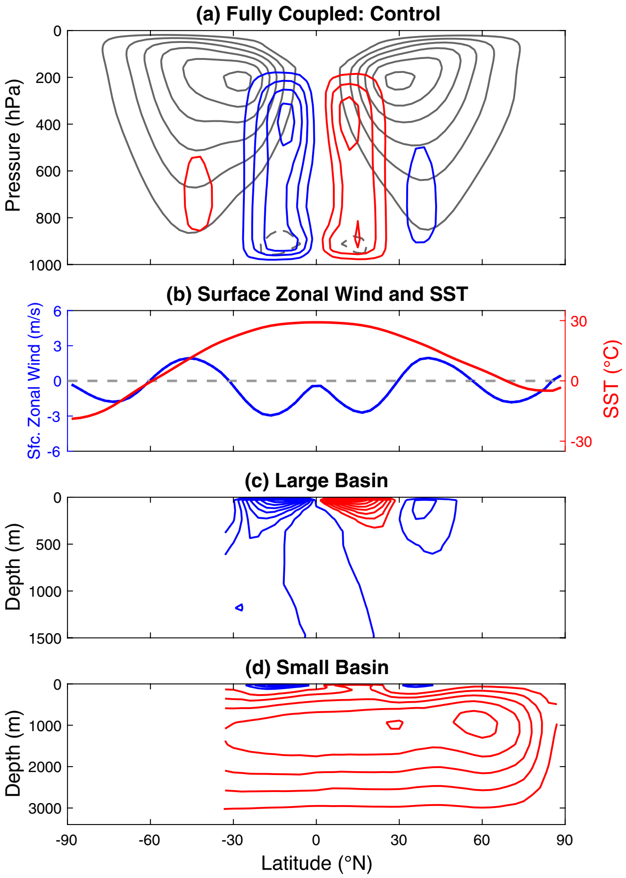

Fig. 3 Zonal mean atmosphere and ocean circulations for the fully coupled control run. **a** Contours of the meridionally overturning streamfunction, with red contours indicating clockwise rotation and blue contours indicating counterclockwise rotation; the contour interval is 30 Sv (1 Sv $= 10^9$ kg s^{-1}). The gray contours indicate the zonal mean zonal wind; the contour interval is 5 m s^{-1}. **b** Zonal mean zonal wind at the model level closest to the surface, located at 993 hPa, and zonal mean sea surface temperature. **c** Contours of the meridionally overturning circulation in the large basin and **d** the small basin, with red contours indicating clockwise rotation and blue contours indicating counterclockwise rotation; the contour interval is 5 Sv. The zero contour is not shown for both the zonal wind and the overturning streamfunctions

slab ocean model configurations, which are spun up for 1000 and 200 years respectively, and the models are then integrated further forward in time for 200 years. All results presented here are averages over the last one hundred years (101–200) after the forcing is applied, at which point the models are in statistical equilibrium. In GM17, the hemispheric energy balance equilibrated (and the contribution by the ocean's heat content tendency to it diminished to zero) roughly 50 years after the forcing was applied (cf. Fig. 5 of GM17). The same is true in these runs where, for the average over years 101–200, the ocean's heat content tendency is an order of magnitude lower than the next smallest term in the hemispheric energy balance, and is also small for all latitudes (not shown). The control runs of the fully coupled and slab ocean configurations are run for a further 100 years after the forced runs are initiated, and time means of the control runs for comparison to the forced responses are taken over these 100 years.

3 ITCZ shifts in the polar-amplified forcing cases

Comparing the responses of the zonal mean precipitation in the fully coupled runs to the slab runs for the polar-amplified forcing (Fig. 4a, b, respectively), the anomalies are significantly damped in the fully coupled case. We define the ITCZ position using the centroid metric of Donohoe et al. (2013), where an area-weighted latitude of zonal mean precipitation is calculated between 20°S and 20°N. The northward shift of the ITCZ in the fully coupled runs is damped relative to the slab runs by a factor of 3.4 in the lowest forcing case, steadily declining to a factor of 2.1 in the highest forcing case. Correspondingly, the anomalous cross-equatorial energy transport by the atmosphere in the fully coupled runs is also reduced, between a factor of 2.5 and 2.7.

Changes in the zonal mean atmospheric circulation are much more dramatic in the slab ocean configuration. The NH Hadley cell in both model configurations has vanished in the highest forcing case (Fig. 5a, d) and replaced by a single large cross-equatorial Hadley cell with a strength of 242 Sv in the fully coupled model and 590 Sv in the slab ocean model. The distributions of zonal mean zonal wind, in both the fully coupled and slab models show similarities, with the NH subtropical westerly jet at roughly 200 hPa being replaced by an eddy-driven extratropical jet. This jet is weaker in the slab ocean configuration, where eddies converge less angular momentum into the jet (not shown), perhaps as a result of the weaker meridional gradient of extratropical SSTs in that model (Fig. 5e). The stronger equatorial easterlies near the tropopause in the slab ocean case are consistent with the larger ITCZ shift, since air ascending in the poleward-displaced ITCZ in the slab runs has lower planetary angular momentum than in the fully coupled runs. Near-surface wind anomalies are correspondingly higher in the slab ocean case, with stronger SH easterly trade wind anomalies and a dramatic reversal of the NH trade winds to westerlies. The surface zonal stress imparted by these westerly winds is in approximate Ekman balance with the northward near-surface flow of the Hadley cell. The weaker cross equatorial Hadley cell in the fully coupled case does not reach the surface in the NH and the zonal winds just north of the equator are weak. Figure 5c, f show that the adjustment of the ocean's overturning cells in both basins results in southward surface cross-equatorial flows and northward anomalous flow below.

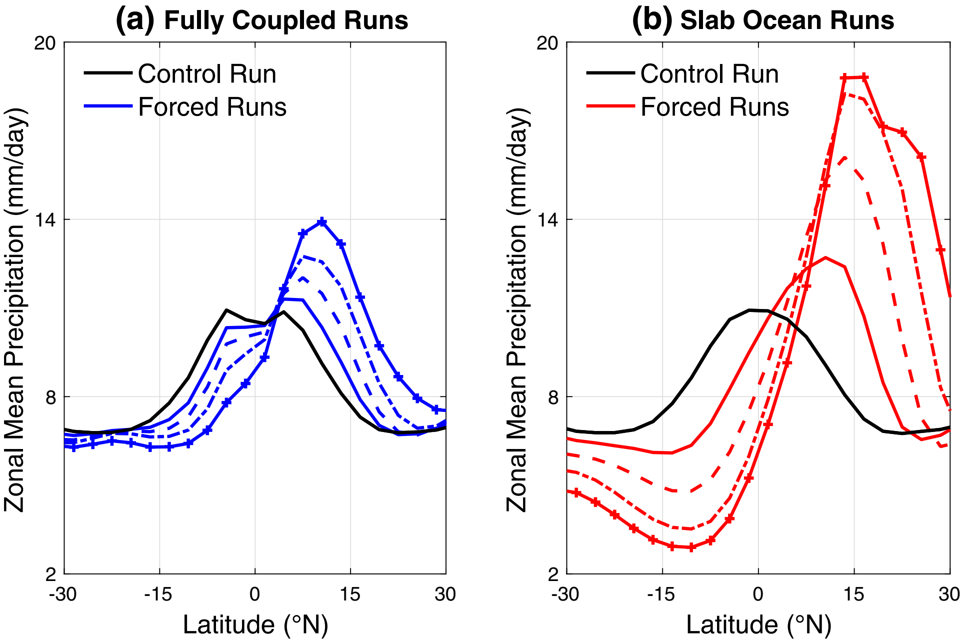

Fig. 4 The precipitation response to the polar-amplified forcing distribution. **a** Annual mean, zonal mean precipitation in the fully coupled runs, with the blue lines indicating the precipitation distributions in response to progressively higher forcing amplitudes. **b** The same, but for the slab ocean runs

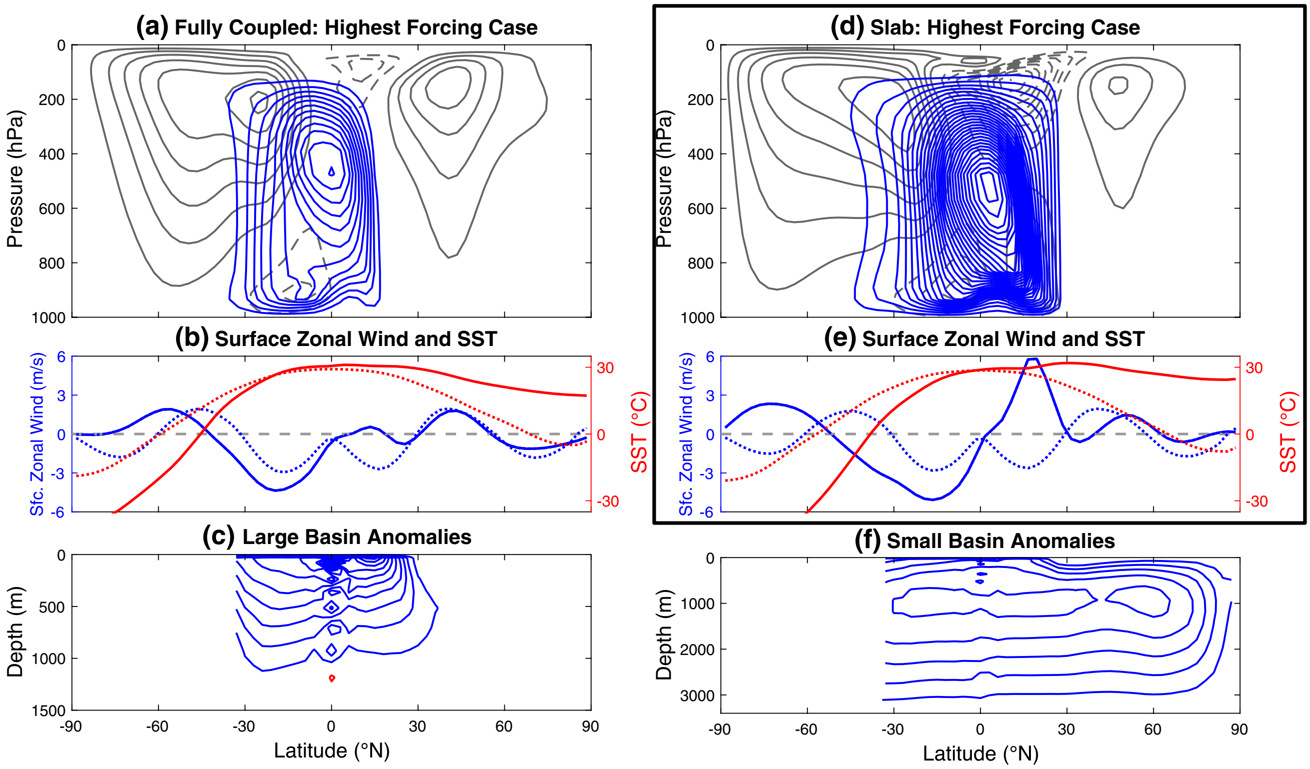

Fig. 5 The response of the zonal mean circulation to the highest amplitude polar-amplified forcing, with the black box indicating slab ocean results. **a** The atmospheric meridional overturning streamfunction in the fully coupled run and **d** the slab ocean run, as in Fig. 3a. Contour interval: 30 Sv and 5 m s^{-1}. **b** The near-surface zonal wind stress and SST in the fully coupled run and **e** slab ocean run, as in Fig. 3b, with the control run distributions plotted as dashed lines. **c** Anomalies of the large basin and **f** small basin overturning streamfunctions. Contour interval: 5 Sv

3.1 The hemispheric energy balance

Contributions to the damped response of the ITCZ shift in the fully coupled case can be diagnosed using the atmosphere's energy balance, which ties the position of the ITCZ to the interhemispheric heating contrast (e.g. Kang et al. 2008, 2009; Donohoe et al. 2013). In a statistically steady state where the atmosphere's and ocean's heat content tendencies can be neglected, any change in the net heating h (in W m^{-2}) of the atmosphere at a given latitude must be balanced by radiative cooling or energy transport divergence. The anomalous radiative cooling can be split into contributions by net shortwave sw or longwave lw radiation at the top of the atmosphere, and the anomalous energy transport divergence split into contributions from the atmosphere's and ocean's northward energy transports, f_A and f_O:

$$h = -sw - lw + \nabla \cdot f_A + \nabla \cdot f_O. \tag{2a}$$

Here, both sw and lw are defined as positive for downward fluxes at the top of the atmosphere to represent heating of the column. The term h represents any externally imposed heating; the terms on the right-hand side represent the adjustment of the climate system. The atmosphere's and ocean's energy transports are diagnosed from the model's dynamical fields, rather than from surface and top-of-atmosphere energy fluxes. Integrating h over both hemispheres and averaging the NH energy balance with the negative of the SH energy balance, Eq. (2a) becomes (in W):

$$H = -SW - LW - F_A - F_O \tag{2b}$$

where F_A and F_O are the atmosphere's and ocean's northward cross-equatorial energy transports. In Eq. (2b), H now represents the anomalous interhemispheric heating contrast, positive if the NH is heated relative to the SH. By modifying the albedo distribution in Fig. 2a, we apply an anomalous interhemispheric heating contrast at the top of the atmosphere, shown in Fig. 2b, where the curves are the imposed anomalous heating h. For our antisymmetric heating distribution, H is equal to the integral of h over the NH, with values of 2.3, 4.7, and 7.0 PW for both forcing distributions, and 9.4 PW for the highest amplitude polar-amplified forcing case. Since our model's atmosphere does not have clouds or absorb shortwave radiation, the adjustment of sw and SW to the prescribed heating is identically zero, though these terms could be included in the energy budget. The values of LW, F_A, and F_O are all anomalies relative to the control run.

On Earth and over the seasonal cycle of our model's control run (Fig. 6a), the relationship between the ITCZ position and the atmosphere's cross-equatorial energy transport is approximately linear, so we can relate the ITCZ shift $\Delta\phi_{ITCZ}$ to F_A by the slope constant b:

$$\Delta\phi_{ITCZ} = -b \cdot F_A. \tag{2c}$$

Over the seasonal cycle, the slope b is 1.8° PW^{-1} in the fully coupled control run; in the slab case control run, it is 2.1° PW^{-1}; on Earth, it is approximately 3° PW^{-1} (Donohoe et al. 2013). Our model has a lower value of b than the Earth for two reasons: an excess of subtropical precipitation that makes the centroid metric less sensitive to shifts in the precipitation maximum, and an ocean that cools the atmosphere at the equator more strongly than it does on Earth (GM17). Since the model's atmosphere does not absorb shortwave radiation, it has an excess of surface heating by that stream relative to Earth, and precipitation rates are higher than they

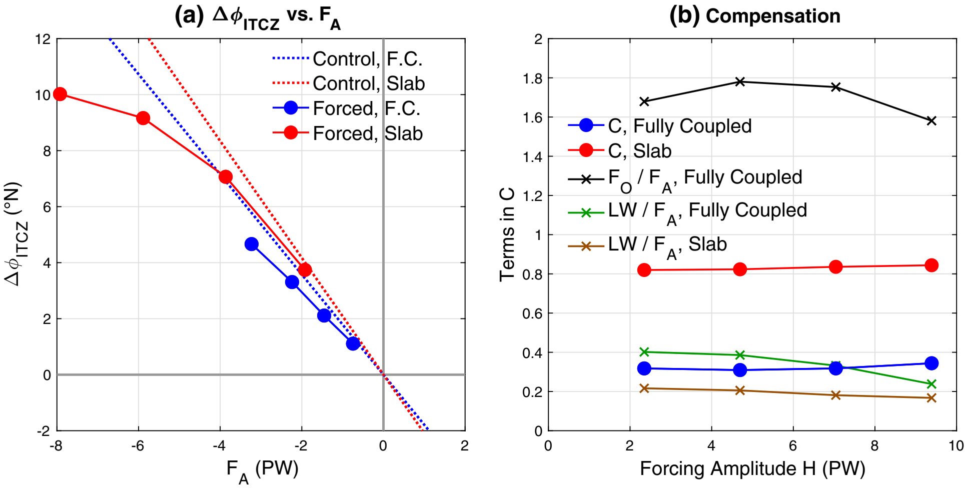

Fig. 6 ITCZ shifts and the hemispheric energy balance for the polar-amplified forcing distribution. **a** The shift in the annual mean ITCZ position relative to the control runs versus the anomalous cross-equatorial energy transport in the atmosphere. Dashed lines indicate a least-squares linear regression of the two quantities' monthly mean climatologies from the fully coupled and slab ocean models' control runs. **b** The degree of compensation and the values of LW/F_A and F_O/F_A in the fully coupled and slab ocean runs, corresponding to the terms in Eq. (3b)

are in the real world. Our model's peak and subtropical precipitation rates in the fully coupled control run are 11 and 7 mm day^{-1}, respectively (Fig. 4a); their values are approximately 6 and 2 mm day^{-1} on Earth. Combining Eqs. (2b) and (2c), the relationship between the ITCZ shift and the interhemispheric heating contrast is:

$$\Delta\phi_{ITCZ} = b \cdot H \cdot C \tag{3a}$$

$$C = \frac{-F_A}{H} = \frac{1}{1 + F_O/F_A + LW/F_A} \tag{3b}$$

where C the "degree of compensation", is the fraction of the interhemispheric heating contrast compensated for by the atmosphere's cross-equatorial energy transport. While the responses of the atmosphere's and ocean's circulations, and radiative fluxes are not easily separable, Eq. (3a) shows how their interplay can affect the response of the ITCZ. If either the heated hemisphere loses more radiation to space (positive LW/F_A), or the ocean transports heat across the equator away from that hemisphere (positive F_O/F_A), the net heating experienced by that hemisphere's atmosphere is reduced. Energy balance then dictates that the atmosphere's cross-equatorial energy transport and ITCZ shift are damped. If, however, the opposite occurs and the responses of the radiative fluxes or ocean energy transport act to amplify the imposed heating contrast (negative LW/F_A or F_O/F_A), the atmosphere has to compensate for a larger fraction of that heating and the ITCZ shifts even further.

The terms in Eq. (3b) are shown in Fig. 6b for each model run versus the magnitude of the imposed heating contrast H. The degree of compensation is typically 0.8 in the slab case but only 0.3 in the coupled cases. This is due in large part to the large F_O/F_A term, representing an offsetting of the imposed heating H by an ocean circulation transporting roughly 70% more energy southward across the equator than the atmosphere. Also contributing to a reduction of the degree of compensation in the fully coupled runs is an increase in LW/F_A, representing an increase in the efficiency of the longwave radiation at offsetting the heating contrast relative to the atmosphere's cross-equatorial energy transport. At lower values of the forcing amplitude, reductions in the slope b in the fully coupled runs (1.5 versus 1.9° PW^{-1} in the slab runs) also act to damp the ITCZ shift, but for the highest forcing case, they amplify it (1.4 versus 1.3° PW^{-1} in the slab runs). Since the terms in the energy balance in Fig. 6b are approximately constant with forcing amplitude, the changes in b explain why ITCZ shifts in the fully coupled runs are less damped at higher forcing amplitudes. Given that F_O/F_A dominates LW/F_A in the energy balance, and is nearly constant with the forcing amplitude, it is clear the large southward cross-equatorial energy transport by the ocean relative to the atmosphere is most responsible for the damping of the ITCZ shifts.

3.2 The ratio of the cross-equatorial energy transports

The largest contributor to the relatively high cross-equatorial energy transport by the ocean in Fig. 6b is the high stratification of the tropical ocean. Splitting the ratio of the oceanic to atmospheric energy transports into the product of the ratio of their mass transports and gross stabilities as in Held (2001) and Czaja and Marshall (2006),

$$\frac{F_O}{F_A} = \frac{\psi_O}{\psi_A} \cdot \frac{c_O}{c_P} \cdot \frac{S_O}{S_A}, \tag{4}$$

the ratios ψ_O/ψ_A and S_O/S_A are shown in red in Fig. 7. By using the specific heat capacity of seawater (c_O, 3994 J kg^{-1} K^{-1}) and the specific heat at constant pressure of dry air (c_P, 1004 J kg^{-1} K^{-1}), the gross stabilities S_O and S_A have units of Kelvin, representing a measure of the temperature contrast between the upper and lower branches of the anomalous circulations. For the atmosphere, this measure of the gross stability represents the temperature contrast between parcels in the upper and lower branches of the circulation if all of their latent heat and potential energy were converted into sensible heat. Though the anomalous ocean circulation is 73–75% weaker than the atmosphere, its gross stability is 54–59% higher (red lines with circles). Compounding the higher temperature contrast of the oceanic circulation is the relatively high heat capacity of seawater; the ratio c_O/c_P is nearly four, making its product with the ratio of the gross stabilities range from 6.1 to 6.3. Thus F_O/F_A in Eq. (4) is 1.6–1.8.

The Hadley cells are responsible for the large majority, 78–82%, of the atmosphere's cross-equatorial energy transport in the fully coupled runs, and their gross stability is within a couple Kelvin of a fit of the seasonal cycle in the control run (Fig. 7b). The Hadley cell's average gross stability over the seasonal cycle in the control run is calculated by regressing its monthly mean climatological cross-equatorial energy transport onto its strength at the equator—the gross stability is the slope of the regression line. The forced runs' annual mean gross stabilities are slightly higher than the fit of the control run's seasonal cycle, but they lie within the range of individual monthly means from the control run's climatology. The ocean's anomalous cross-equatorial energy transport is accomplished by two distinct circulations: a shallow, wind-driven CEC confined to the thermocline in the large basin (Fig. 5c), and a deep overturning circulation in the small basin (Fig. 5f), making the oceanic gross stability plotted in Fig. 7b slightly unintuitive. Splitting the cross-equatorial energy transport into its small basin and large basin components and calculating the gross stability for each, both are lower than the global mean since the mass transport anomalies in each basin peak at different depths.

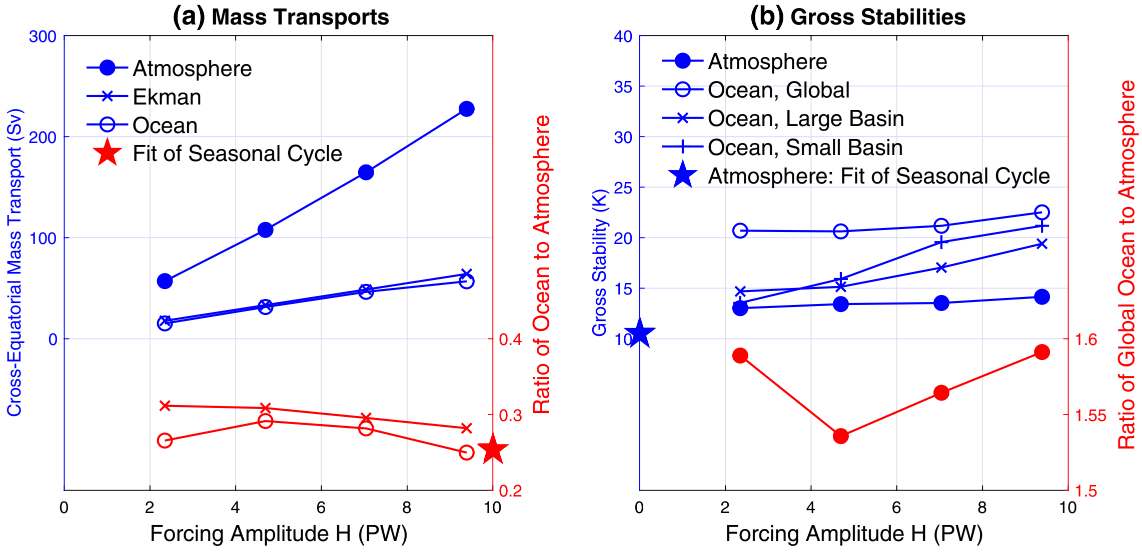

Fig. 7 Contributions to the atmosphere's and ocean's cross-equatorial energy transports in the fully coupled model runs for the polar-amplified forcing distribution. **a** Annual mean mass transport anomalies (blue), taken as the peak meridional overturning streamfunction anomaly at the equator in the atmosphere and an average of peak anomalies at 6°N and 6°S in the ocean. The Ekman transport is calculated using the surface wind stress anomalies at 6°N and 6°S, integrating the resulting Ekman transport in longitude, and averaging the two values. The ratio of the ocean and Ekman mass transport anomalies to the atmosphere's is shown in red. The Ekman-atmosphere ratio in the fully coupled control run, indicated with a star, is estimated as a least-squares regression of monthly mean climatological Ekman transport onto the atmospheric mass transport. **b** Gross stabilities (blue), calculated as the ratio of the anomalous cross-equatorial energy and mass transports, divided by the heat capacity. The Hadley cell's gross stability in the fully coupled control run, indicated with a star, is estimated as the slope of the least-squares regression at the equator of the atmosphere's monthly mean climatological energy transport onto its mass transport. The ratio of the atmosphere's to the global ocean's gross stability is shown in red

The peak mass transport anomaly of the global zonal-mean ocean is then weaker than the sum of the two basins' peak mass transports, artificially increasing the global ocean's gross stability. Both basins' gross stabilities, though, are higher than the atmosphere's for all forcing amplitudes.

As the forcing amplitude increases, the gross stability of the large basin's CEC increases, from 15 to 19 K. The structure of the CEC, though, does not significantly change with the forcing amplitude, with southward-flowing surface water subducted in the SH extratropics returning northward in the thermocline. With the lower branch water conserving temperature as it flows northward, the gross stability of the CEC at the equator in our simulations is set by the SST contrast between the equator and the SH surface westerly jet, as in GM17. As the forcing amplitude increases, SH extratropical SSTs decrease (Fig. 5b) and the gross stability of the CEC increases.

In the small basin, circulation anomalies are dominated by a weakening of the deep MOC, which shuts down completely in the highest forcing case and is replaced by a shallower CEC of the type seen in the large basin. With a large fraction of its upper branch inside the thermocline and its lower branch in the weakly stratified deep ocean (Fig. 3d), the deep MOC has a gross stability of 11 K in the control run, smaller than an anomalous CEC in the large basin. As the small basin's deep MOC weakens and its shallower CEC strengthens, the temperature contrast between the upper and lower branches of the circulation increases; the gross stability increases from 14 K in the lowest forcing case to 21 K in the highest forcing case. In the highest forcing case, the anomalous circulation's gross stability is higher than the large basin's and is set by the difference between equatorial SSTs and the temperature of the deep ocean, rather than the temperature difference across the thermocline (Fig. 5f). The shift from a deep MOC to a shallow CEC in the small basin varies the fraction of its contribution to F_O as the forcing amplitude increases. For the three weakest forcing amplitudes, each basin contributes nearly equally to F_O. For the highest forcing amplitude, the small basin's contribution reduces to 43% because the deep MOC can no longer weaken and because the 90°-wide small basin's shallow CEC is weaker than its counterpart in the 270°-wide large basin.

Although it is constrained to overturn in the same sense as the atmosphere's circulation by its coupling to the trade winds, the tropical ocean circulation is not constrained to have the same strength, and its anomalies are weaker in our simulations (Fig. 7a). Similar to GM17, the anomalous cross-equatorial ocean circulation in these simulations is approximately in Ekman balance with the surface wind stress, nearly matching the Ekman mass transport calculated from zonal wind stress anomalies averaged at 6°N and 6°S. The Ekman transport, confined to a near-surface frictional layer in the ocean and atmosphere, is weaker than the total atmospheric overturning anomaly, which peaks in the mid-troposphere (Fig. 8a). For the atmospheric and oceanic mass transports to be identical, the peak atmospheric overturning anomaly would have to extend down to the top of this layer, located at approximately 900 hPa in our model.

The atmosphere's angular momentum balance, where the divergence of angular momentum transport by the Hadley cells and eddies is balanced by torques associated with surface friction and pressure torques (e.g. Peixoto and Oort 1992, Eqs. 11.12–13), dictates the strength of the trade winds and the resulting oceanic overturning circulation. Integrating the balance zonally and vertically and neglecting the influence of surface pressure torques, the momentum tendency is equal to the divergence of the meridional flux of relative angular momentum by the atmospheric circulation, minus the torque due to the wind stress:

$$2\pi R cos\phi \int_0^{P_S} \overline{\frac{\partial}{\partial t}[M]}\frac{dP}{g} = -2\pi R \int_0^{P_S} \frac{\partial}{\partial \phi}\left(cos^2\phi\left([\bar{u}][\bar{v}] + [\bar{u}^*\bar{v}^*] + \left[\overline{u'v'}\right]\right)\right)\frac{dP}{g} - 2\pi R cos\phi\left[\overline{\tau_x}\right]. \tag{5}$$

Overbars indicate time averages, primes indicate departures from the time mean, square brackets indicate zonal mean quantities, and asterisks indicate departures from the zonal mean. The angular momentum is represented by M, u and v are the zonal and meridional velocities, P_S is the surface pressure, R is the radius of the Earth, g is the acceleration due to gravity, ϕ is latitude, and τ_x is the zonal wind stress. Surface pressure torques cannot be generally neglected in the momentum balance but, since our model's surface is flat, they can be here. The terms in Eq. (5) are in units of force, or torque per unit length latitude, and the angular momentum flux divergence is split into contributions by the time mean, zonal mean circulation (the Hadley cells), stationary waves, and transient circulations.

The anomalous oceanic CEC in our simulations is driven by a hemispherically asymmetric pattern of surface zonal wind stress, so in Fig. 8b we plot the difference between the torques at 6°N and 6°S exerted on the atmosphere by the zonal wind stress anomalies, and the convergence of angular momentum transport by the Hadley cells. Over both the seasonal cycle in the control run and in the annual mean of the forced runs, the two nearly perfectly balance each other, and the effects of eddy momentum transport are small. That both the annual mean angular momentum balance and the mass transport ratio ψ_O/ψ_A in the forced runs closely match the seasonal cycle in the control run (Fig. 8b; red star, Fig. 7a) suggest that the mass transport ratio can be predicted by the seasonal cycle of the Hadley cells, without accounting for the effects of eddy angular momentum

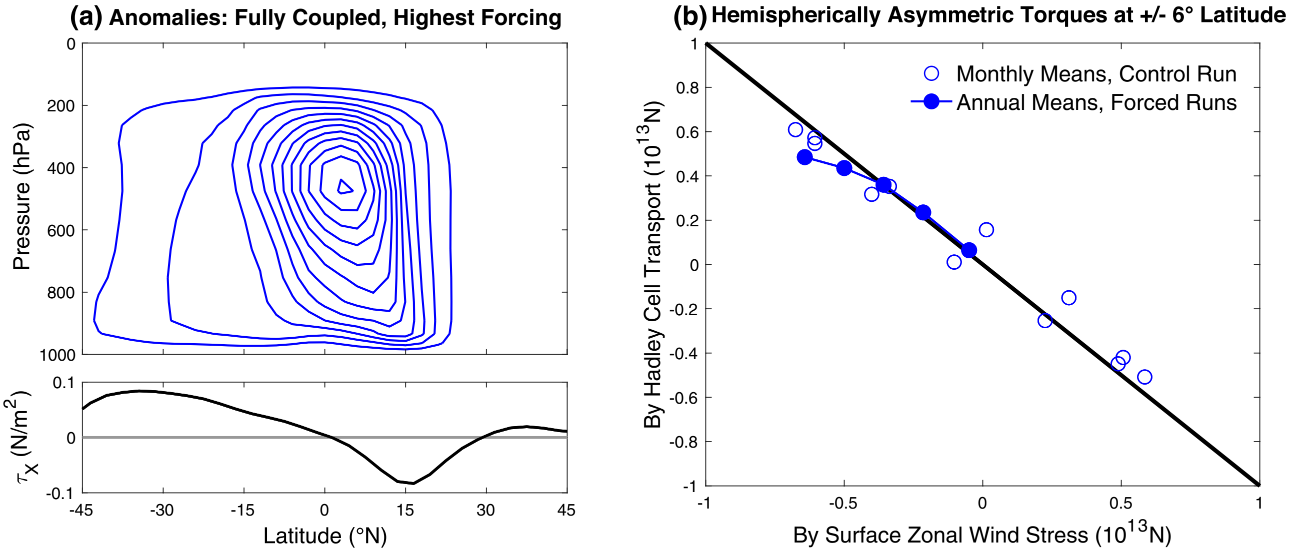

Fig. 8 The atmosphere's angular momentum balance in the fully coupled model for the polar-amplified forcing distribution. **a** Anomalies in the highest forcing case in the meridional overturning streamfunction (top, contour interval: 20 Sv) and the surface zonal wind stress on the atmosphere (bottom). **b** The difference between the integrated (vertically and zonally) torques on the atmosphere at 6°N and 6°S, with positive values indicating a positive torque on the northern hemisphere atmosphere relative to the southern hemisphere. The y-axis is the convergence of angular momentum transport by the time mean, zonal mean circulation, and the x-axis is the torque exerted by the zonal mean zonal wind stress at the surface

transport. It is also worth noting that as long as the oceanic CEC is in Ekman balance with the surface wind stress, its strength may increase and approach that of the anomalous Hadley cell, but it can never be stronger and the ratio ψ_O/ψ_A cannot exceed unity.

3.3 The ocean's impact on the radiative response

The increased longwave radiative efficiency LW/F_A in the fully coupled runs (Fig. 6b) also contributes to the damping of ITCZ shifts, although the effect is small relative to F_O/F_A. Per Petawatt of cross-equatorial atmospheric energy transport, the NH in the fully coupled runs is fluxing nearly double the anomalous longwave radiation to space than it is in the slab runs for all the forcing amplitudes. This increase in the efficiency of the longwave radiation can be understood by returning to the atmosphere's energy balance. Modifying Eq. (2a) by incorporating the convergence of the ocean's heat transport into the left-hand side to define a "net heating" of the atmosphere, $h_{net} = h - \nabla \cdot f_O$, the atmosphere's energy balance at a given latitude is:

$$h_{net} = -lw - sw + \nabla \cdot f_A. \tag{6a}$$

In the slab ocean runs, there is no change in the ocean heat transport convergence and $h_{net}=h$. Since sw is zero for our simulations, the response of the atmosphere to the combination of the albedo forcing and anomalous ocean heat transport convergence is a balance between outgoing longwave radiation at the top of the atmosphere and atmospheric energy transport divergence. An integral of Eq. (6a) over a hemisphere, analogous to Eq. (2b), yields a balance between the hemisphere's net heating, its net outgoing longwave radiation LW, and the atmosphere's cross-equatorial energy transport F_A. The increase in LW/F_A in the fully coupled runs indicates a shift in the atmosphere's response from the latter to the former and, we will argue, is a result of the ocean's heat transport modifying the meridional profile of the net heating of the atmosphere.

The meridional profiles of net heating can be compared between the simulations by normalizing Eq. (6a) by the northern hemisphere's average net heating (the SH average is the same magnitude but opposite sign):

$$\frac{h_{net}}{h_{net,mean}} = \frac{-lw}{h_{net,mean}} + \frac{\nabla \cdot f_A}{h_{net,mean}}. \tag{6b}$$

These normalized profiles are plotted in Fig. 9a versus the sine of latitude to area-weight the distribution. All of the slab ocean cases collapse onto a single line taking the shape of the albedo forcing, and it is notable how similar the fully coupled cases are given the range of forcing amplitudes. Comparing the two sets of curves, the effect of the ocean's heat transport in the fully coupled runs is to concentrate the net heating at higher latitudes; in the tropics, heating in the NH has changed to cooling and cooling in the SH has changed to heating.

The redistribution of net atmospheric heating in the fully coupled runs to higher latitudes is due to the mismatch of the profiles of the albedo-forced heating and the ocean's anomalous heat transport convergence and resulting surface heat fluxes. The heating driven by the albedo changes is strongly polar-amplified, but roughly half of the ocean's anomalous

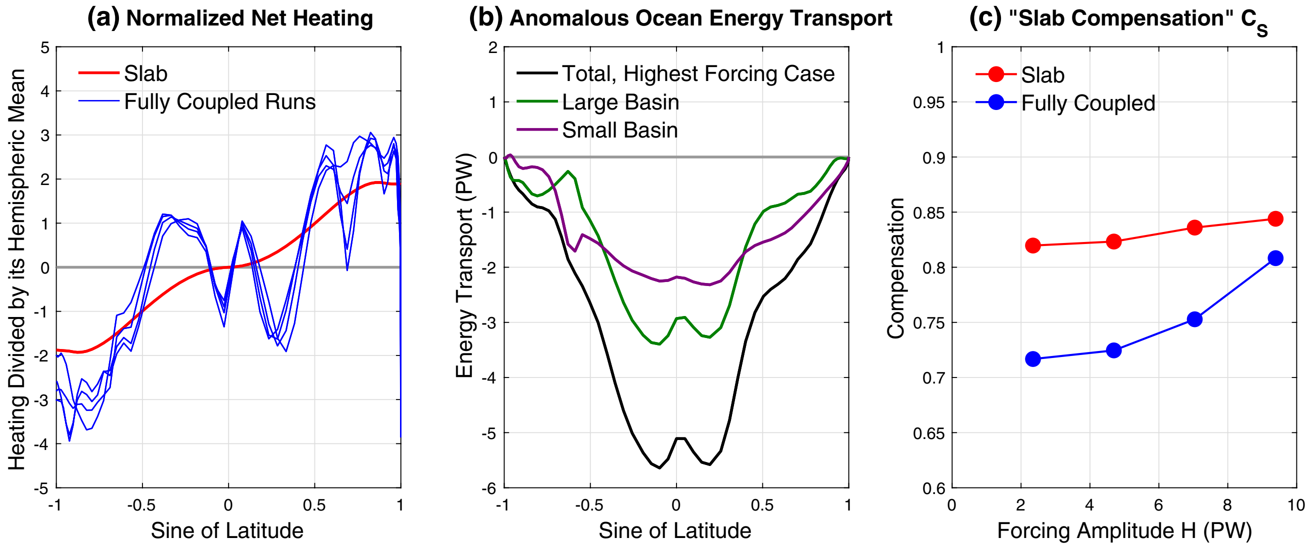

Fig. 9 The effect of the ocean on the atmosphere's radiative fluxes for the polar-amplified forcing distribution. **a** Normalized net heating of the atmosphere, following Eq. (6b). **b** Anomalous ocean energy transport in the fully coupled, highest forcing case. **c** The atmosphere's degree of compensation for the "net heating" it experiences, following Eq. (6c)

cross-equatorial heat transport is diverged or converged equatorward of 30° (Fig. 9b), heating and cooling the atmosphere at latitudes where the imposed heating is weak. In the highest forcing case, 64% of the large basin's cross equatorial heat transport is converged/diverged equatorward of 30°, varying by only a couple percent for the other forcing amplitudes. Because the large basin's anomalous heat transport is coupled to the atmospheric circulation above, the redistribution of a polar-amplified heating profile further poleward by the type of wind-driven CEC described in GM17 appears to be a robust feature of the climate's response.

By itself, a change in the distribution of the net heating profile is not sufficient to alter the balance between the hemispheric mean longwave radiative flux and atmospheric cross-equatorial energy transport. For that balance to change, the atmosphere's partitioning of its response between radiative fluxes and energy transport divergence must also have a meridional dependence. In our simulations, the longwave radiative feedback (defined as the negative of the change in outgoing longwave radiation at the top of the atmosphere divided by the change in SST) is positive when SSTs and longwave radiation anomalies in each hemisphere are averaged between the equator and 30° latitude, and negative when averaged between 30° and the poles. This indicates the relative efficiency of the extratropical atmosphere at radiating heating anomalies away to space. Our gray radiation model only has Planck, lapse rate, and water vapor feedbacks, of which only the water vapor feedback is positive, and the net positive tropical radiative feedback can be attributed to the relatively high concentrations of water vapor there.

With our model's atmosphere able to radiate heating anomalies to space more efficiently at high latitudes, by concentrating the profile of the net heating of the atmosphere there, the ocean increases the relative contribution of longwave radiative fluxes to equilibrating the atmosphere's energy balance. This effect can be related to the ratio LW/F_A by integrating Eq. (6a) over a hemisphere and dividing by F_A. Re-arranging the terms gives:

$$\frac{LW}{F_A} = \frac{1}{C_S} - 1, \tag{6c}$$

$$C_S = \frac{-F_A}{H_{net}} = \frac{-F_A}{H + F_O}, \tag{6d}$$

where C_S is the "slab compensation," the degree of compensation expected in a slab ocean model if it was presented with the forcing distribution h_{net}. Equation (6c) is equivalent to Eq. (3b) if F_O/F_A was removed from the denominator and F_O was added to H. Since the profiles of net heating in Fig. 9a are further polar-amplified in the fully coupled runs and the atmosphere more efficiently radiates heating anomalies to space at those latitudes, C_S decreases compared to the slab ocean runs (Fig. 9c) and LW/F_A increases. This result is consistent with previous modeling studies with a slab ocean GCM, where C_S was lower for forcing distributions that were polar-amplified (Seo et al. 2014; Kang et al. 2014). Moreover, in simulations of global warming, patterns of ocean heat uptake interacting with radiative feedbacks have been shown to alter the equilibrium climate sensitivity (Rose et al. 2014). Our results reinterpret this effect for interhemispheric forcing.

3.4 The relationship between the ITCZ position and the atmosphere's cross-equatorial energy transport

The connections between the ocean circulation and the slope of the $\Delta\phi_{ITCZ}$–F_A relationship are less direct and vary with the forcing magnitude. Differences in the slope can be interpreted as a measure of how efficiently the atmosphere moves energy across the equator: to accomplish a given cross-equatorial energy transport and equilibrate its energy budget, a lower value of b means that the atmosphere doesn't have to shift the ITCZ as far.

For a given atmospheric cross-equatorial energy transport F_A, the slope b is always reduced in the fully coupled runs (solid lines, Fig. 10a). As the forcing amplitude increases in the slab ocean runs and the magnitude of F_A increases past its maximum in the fully coupled runs, b reduces as the atmosphere becomes more efficient at moving energy southward across the equator. This is perhaps to be expected, particularly at high forcing amplitudes, if the Hadley cells enters a non-linear, angular momentum conserving regime and the strength of the cross-equatorial cell increases super-linearly with the latitude of the ITCZ (Lindzen and Hou 1988; Plumb and Hou 1992). Indeed, as the ITCZ moves further northward in the slab runs, the strength of the anomalous cross-equatorial Hadley cell increases super-linearly with its position, but the relationship remains linear for the smaller ITCZ shifts in the fully coupled runs (not shown). The apparent amplification of ITCZ shifts at high forcing amplitudes by the ocean circulation's effect on b, then, is artificial—the high ITCZ shifts in the slab ocean runs are only realized without the damping effect of the ocean's cross-equatorial energy transport.

At lower forcing amplitudes and values of F_A, b is consistently lower in the fully coupled runs, contributing to the damping of the ITCZ shift. Comparing the precipitation distributions for similar values of F_A (-2.2 PW in the fully coupled case versus -1.9 PW in the slab case; Fig. 10b), part of the reason for the lower slope in the fully coupled run are the higher precipitation rates in the subtropics. The centroid metric we use is an area-weighted latitude of precipitation between 20°S and 20°N, and the increases in precipitation

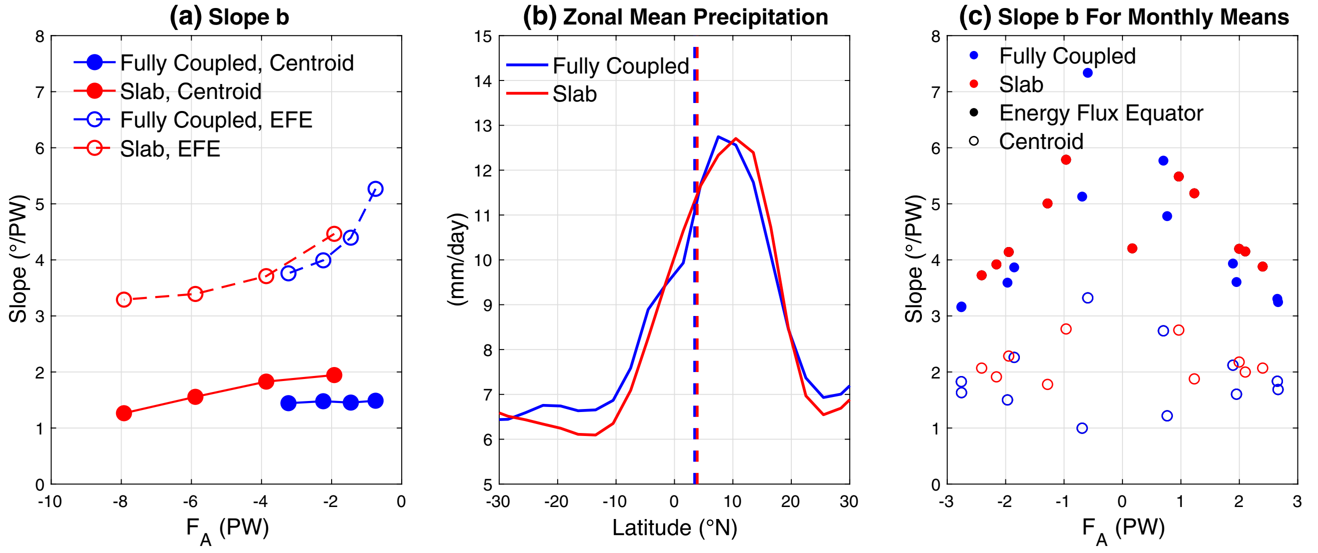

Fig. 10 The slope of the $\Delta\phi_{ITCZ}$–F_A relationship for the polar-amplified forcing distribution. **a** For the centroid metric (solid) and energy flux equator metric (dashed), versus the atmosphere's anomalous cross-equatorial energy transport. **b** Zonal mean precipitation distributions for the fully coupled model's second-highest forcing amplitude case and the slab ocean model's weakest forcing case. Dashed lines indicate the ITCZ positions, calculated using the centroid metric. **c** The slope b calculated from monthly mean climatologies of the fully coupled and slab ocean models' control runs, for both the centroid metric and the energy flux equator metric

between 5°S and 20°S project onto a southward shift of the metric relative to the slab case. This increase in subtropical precipitation in the fully coupled model is also seen when comparing its highest forcing case to the slab model's second-lowest forcing case.

Since we are focusing on changes in the position of the ITCZ, rather than in subtropical precipitation rates, we compare the results using the centroid metric to those where the position of the ITCZ is defined as the latitude where the atmosphere's northward energy transport vanishes, termed the energy flux equator (EFE; Kang et al. 2008). By using the atmosphere's energy transport distribution to define the ITCZ position, the EFE metric is more closely related to the atmosphere's energy balance than the centroid metric, at the cost of not being directly related to changes in precipitation.

For all forcing amplitudes, the slope b using the EFE metric is higher in the fully coupled runs relative to the slab ocean runs (Fig. 10a), implying an amplification of the ITCZ shift in the fully coupled case. However, we again see that this is because of a dependence of b on the magnitude of F_A. In the EFE estimation of the ITCZ position, the curvature of the atmosphere's northward energy transport with latitude plays a non-negligible role once the ITCZ moves more than a couple degrees from the equator (Bischoff and Schneider 2016). In agreement with the annual mean response of the forced runs, we also see a dependence of monthly mean values of b on F_A for both the fully coupled and slab ocean models' control runs (Fig. 10c). However, this same dependence of b on F_A over the control runs' seasonal cycles is not seen if the centroid metric is used.

At a given value of the atmosphere's cross-equatorial energy transport F_A, there appears to be a reduction in the slope b using the EFE metric for the fully coupled runs. Again comparing the lowest-forcing slab case to the second-highest forcing fully coupled case, b is reduced by 11%. In the EFE framework, this means that the atmosphere is diverging more heat between the ITCZ position and the equator in the fully coupled run, steepening the slope of its northward energy transport distribution as a result of a net input of energy into the region. Comparing the two runs between the equator and 9°N, the approximate latitude of the ITCZ in both cases, there is an increase in the net upward surface energy flux of 5.2 W m^{-2} in the fully coupled run, of which 23% is compensated by an increase in the outgoing longwave radiation at the top of the atmosphere. The rest of that heating is diverged by the atmosphere, steepening the slope of its energy transport curve and reducing the value of b. This local increase in the upward surface heat flux is a result of a convergence of the ocean's heat transport, seen just north of the equator in Fig. 9b, and is connected to a reduction in the ocean's anomalous southward heat transport right at the equator. Across all forcing amplitudes, similar reductions in the southward heat transport at the equator occur in the fully coupled runs, and are related to a sinking and cooling of some of the surface wind-driven flow as it crosses the equator (see GM17). A similar effect has been seen in experiments with a slab ocean GCM incorporating

Ekman dynamics only (Kang et al. 2018b). As a consequence of the equatorial structure of the wind-driven CEC, a reduction in the slope *b* and a damping of ITCZ shifts appears to be a robust feature of the fully coupled runs.

4 Forcing confined to the tropics

To test the robustness of the ocean circulation's damping effect on ITCZ shifts, we compare the previous section's results to those where the forcing is confined to the tropics. By limiting the albedo adjustments to the tropics, these runs' heating profiles (Fig. 2b) have larger gradients than the polar-amplified distributions, increasing in amplitude from zero at the equator, peaking at 14.5° latitude and decaying to zero at 30° latitude. It is difficult to imagine a realistic interhemispheric forcing of this magnitude that is confined to the tropics, particularly for a fully coupled atmosphere–ocean system, but the response of our model to these idealized forcing distributions provides a useful contrast to the polar-amplified distributions discussed above.

The resulting ITCZ shifts (Fig. 11a) are still damped in the fully coupled runs relative to the slab ocean runs, but by a smaller amount than they are for the polar-amplified forcing distribution. From the smallest amplitude forcing case to the largest amplitude case, the ratio of the slab to fully coupled runs' ITCZ shifts decreases from 1.7 to 1.5, lower than the 3.4–2.8 range for the same forcing amplitudes in Fig. 6a. The atmosphere in the fully coupled runs also transports a larger fraction of the forcing southward across the equator; the degree of compensation *C* by the atmosphere's cross-equatorial energy transport ranges from 0.63 to 0.66 (Fig. 11b), compared to a range of 0.31–0.34 in Fig. 6b. The slab ocean runs' range of *C*, 1.00–1.02, is also higher in these runs than before, but the relative increase in *C* in the fully coupled runs is higher.

The largest contributor to the reduction in the damping of ITCZ shifts is a reduction in the ocean's cross-equatorial energy transport. Smaller contributions come from changes in the compensation by longwave radiation and the slope *b*. The ocean's cross-equatorial energy transport is roughly 60% of the atmosphere's in these runs (Fig. 11b), much lower than before (Fig. 6b), and there are now only minimal changes in LW/F_A between the slab ocean and fully coupled runs. For a given forcing amplitude, changes in *b* between the fully coupled and slab runs are small, whereas for similar polar-amplified forcing amplitudes they contribute to a larger fraction of the damping. The consequence of the small changes in LW/F_A and *b* is that the ocean's anomalous cross-equatorial energy transport, lower than it was in the polar-amplified forcing cases, is the sole agent acting to damp the ITCZ shift in the fully coupled runs.

4.1 Ocean circulation and energy transport anomalies

The most noticeable difference in the ocean's circulation, compared to the polar-amplified forcing cases, is the relatively small change in the small basin's deep MOC, even in the highest forcing case (Fig. 12f). Instead of a weakened deep MOC transporting heat anomalously southward across the equator, as in Fig. 5f, the largest streamfunction anomalies in the small basin are confined to the thermocline, similar to the large basin (Fig. 12c). Both basins'

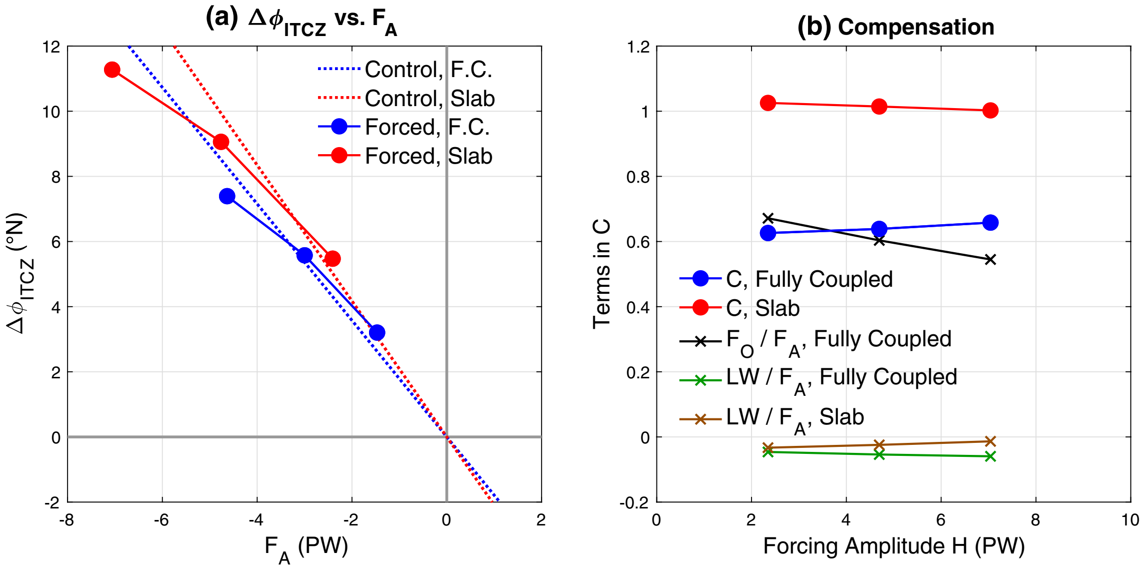

Fig. 11 ITCZ shifts and the hemispheric energy balance, as in Fig. 6, for the tropics-only forcing distribution

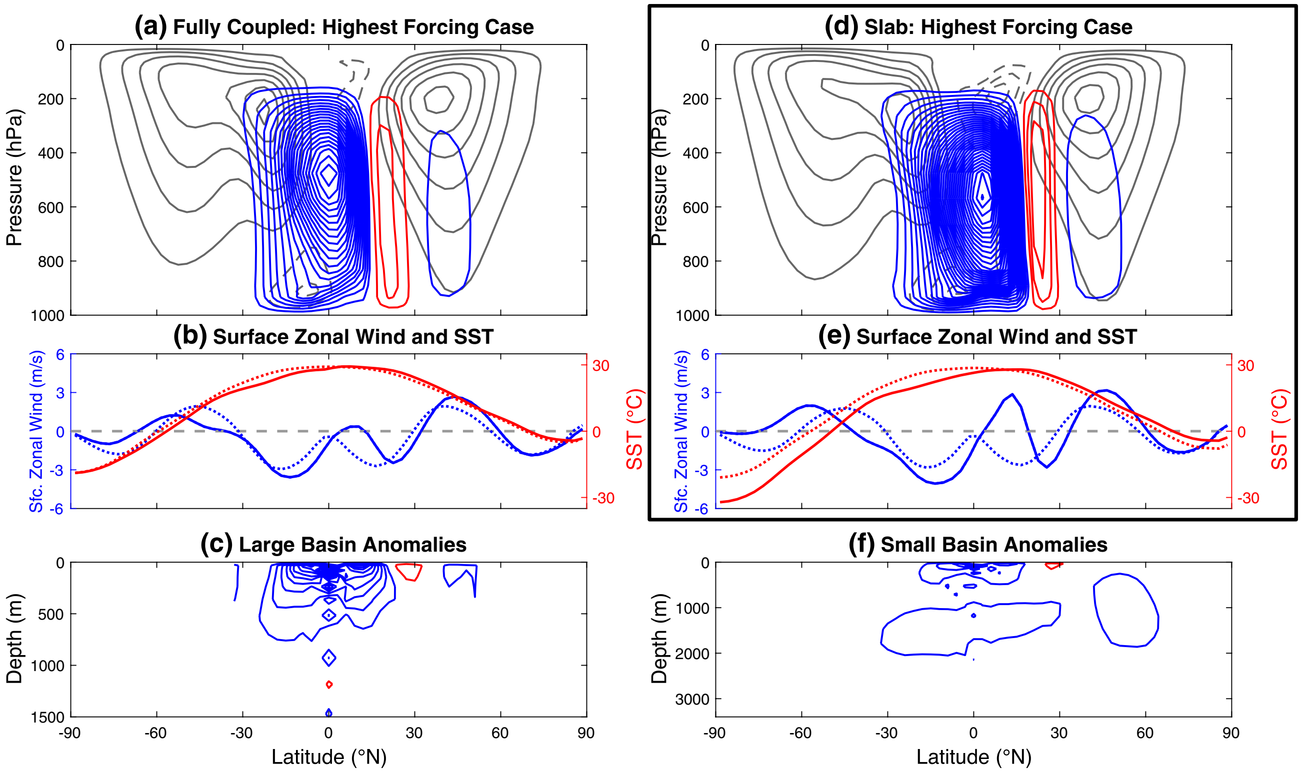

Fig. 12 The response of the zonal mean circulation, as in Fig. 5, to the highest amplitude tropics-only forcing

anomalous circulations are surface-intensified CECs like those described in Sect. 3.2, driven by the surface zonal wind stress anomalies and transporting heat southward across the equator due to the temperature contrast between the surface and return branches. The small basin/large basin split of the ocean's cross-equatorial energy transport is 30/70% for all forcing amplitudes, reflecting the relative sizes of the basins. The reduced fraction of cross-equatorial heat transport accomplished in the small basin is partially responsible for the reduction of the total oceanic transport and the reduced F_O/F_A: without a weakening of the deep MOC, the size of the small basin limits the heat transported by its wind-driven CEC.

The pattern of surface zonal wind anomalies (Fig. 12b) are more localized for the tropics-only forcing distribution, and the anomalous wind-driven CECs in both basins are confined to within roughly 20° latitude of the equator. Rather than supplying the CECs with water pumped downward in the extratropics due to a southward shift of the SH surface westerly jet, as in Fig. 5b, the surface wind anomalies in Fig. 12 reflect a more local northward shift of the trade winds in the tropics. Reduced eddy momentum fluxes in the SH extratropics (not shown) weaken the SH surface westerly jet, but the jet does not shift and anomalies in the trade winds and resulting meridional Ekman transport switch sign at 20°S. This reduction in the CEC widths relative to the polar-amplified forcing runs leads to the reduction in their gross stabilities, warming and shoaling the deep western boundary current comprising the cell's subsurface return branch. Both the large and small basin wind-driven CECs have a gross stability of 12 K, reduced from 15 to 19 K for the large basin in Fig. 7b, that does not vary strongly with the forcing amplitude since SST anomalies are weaker in these runs (compare Fig. 12b to Fig. 5b). The warming of the boundary current due to Ekman pumping at lower latitudes is partially responsible for the reduction of the ocean's cross-equatorial energy transport relative to the atmosphere.

Though clearly driven by the surface wind stress anomalies, the CECs in the tropics-only forcing runs are weaker than circulations in Ekman balance with those anomalies would be. The strength of the cross-equatorial mass transport in these runs is only 61–63% of the implied Ekman transport, compared to 85–95% for the polar-amplified forcing runs in Fig. 7a. Diagnosing the model's zonal momentum balance in the surface layer, the zonal wind stress anomalies in these runs are partially offset by the horizontal diffusion of zonal momentum. As a result, the Coriolis acceleration on the meridional flow is weaker than it would be if the surface flow was in Ekman balance. The horizontal viscosity in the momentum equation for this version of the MITgcm ocean model is a spatially uniform 3×10^5 m^2 s^{-1}, similar to other ocean general circulation models in the tropics (e.g.

Griffies et al. 2005), following the Munk scaling for western boundary currents (Munk 1950). However, most of the dissipation of anomalous zonal momentum in these runs occurs in the interior of the basins, and this type of diffusion-driven weakening of the CECs is likely unphysical. By confining the anomalous CECs to a narrower range of latitudes, gradients in surface currents resulting from the more local wind stress anomalies are higher, and the model more strongly dissipates those currents' momentum. Through Eq. (4), the reduction in the CECs' mass transport anomalies relative to the atmosphere compounds their reduced gross stability and reduced small basin heat transport, contributing to the lower F_O/F_A values in the tropics-only forcing cases.

4.2 Changes in LW/F_A and the slope b

The response of the longwave radiation is very similar in the slab ocean and fully coupled runs (Fig. 11b), and LW/F_A is smaller than in the polar-amplified forcing runs (Fig. 6b). By concentrating the forcing in a region where the radiative feedbacks in our model are positive, the tropics-only forcing distribution results in small negative values of LW/F_A. The similar values of LW/F_A in the slab ocean and fully coupled runs are related to the distribution of net heating in the atmosphere (Fig. 13a): though the ocean reduces the interhemispheric heating contrast, it does not significantly modify its distribution. The anomalous cross-equatorial energy transport in both basins' narrower CECs is diverged and converged almost entirely within 25° of the equator, in close alignment with the forcing distribution, preventing its interaction with the model's spatial pattern of radiative feedbacks from altering LW/F_A.

The weak damping of the ITCZ shifts by changes in the slope b in the fully coupled runs is again found to be more pronounced when b is plotted versus F_A (Fig. 13b). The causes of the reduction in b, for both the centroid and EFE metrics, in the fully coupled runs are identical to those discussed in Sect. 3.4. Subtropical SH precipitation is similarly reduced when slab and fully coupled runs with similar F_A are compared (not shown), and a reduction in the ocean's anomalous southward heat transport at the equator again leads to a heating of the atmosphere just north of the equator. Though it is not the primary mechanism by which the ocean damps ITCZ shifts, a reduction in the slope of the ITCZ position-atmospheric cross-equatorial energy transport relationship appears to be robust.

5 Discussion of the role of the CEC in the atmosphere's energy balance

In our simulations, the ocean accomplishes its cross-equatorial energy transport by "wrapping" a cross-equatorial cell around the STCs, with its lower branch crossing the equator at colder temperatures than the STCs' lower limbs. By crossing the equator in a frictional western boundary current, the CEC's lower branch is able to reverse the sign of its potential vorticity. Our results disagree with the type of ocean circulation envisaged by Schneider (2017) which, as schematized in his Fig. 2, suggests that the ocean accomplishes its

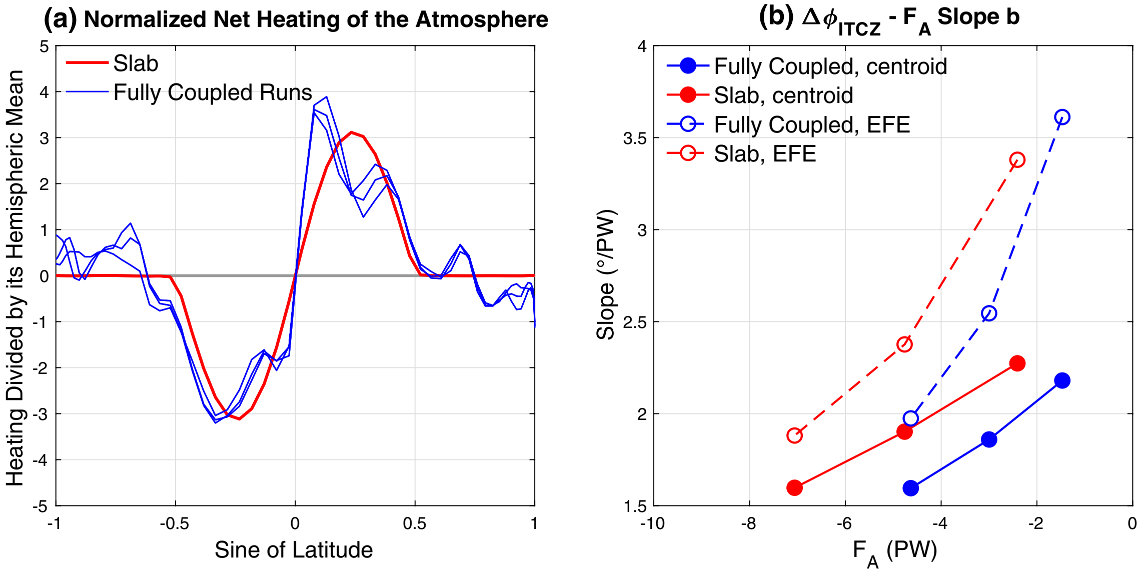

Fig. 13 The effect of the ocean on the atmosphere's radiative fluxes and slope b in the tropics-only forcing cases. **a** Normalized net heating of the atmosphere, following Eq. (6b), as in Fig. 9a. **b** The slope b calculated using the energy flux equator and centroid metrics, versus the atmosphere's anomalous cross-equatorial energy transport, as in Fig. 10a

cross-equatorial energy transport by shifting the upwelling zone along with the ITCZ. For a northward ITCZ shift, this would result in a cross-equatorial SH subtropical cell that mirrors its counterpart Hadley cell. Though the latitude of mean ascent in the atmosphere shifts with the ITCZ, the tropical ocean's upwelling zone never shifts off of the equator, as can be seen in Fig. 14. For both polar-amplified and tropics-only forcing distributions, vertically averaged ascent in the atmosphere is shifted into the NH (solid black contours) along with the ITCZ, but the ocean's upwelling zone (red colors) remains on the equator. The highest amplitude forcing cases are presented in Fig. 14, but this behavior is seen for all forcing amplitudes. We suggest that the tropical ocean circulation associated with a northward ITCZ shift is more accurately schematized in Fig. 1: instead of the upwelling zone shifting to the latitude of the ITCZ, southward cross-equatorial flow at the surface is balanced by a northward flow in the thermocline below the STCs. The southward cross-equatorial surface flow does not imply a shift in the upwelling zone and distribution of surface divergence; rather, it is the addition of a constant southward flow throughout the tropics to the background divergent flow.

Anchoring the upwelling zone to the equator is a surface zonal wind stress distribution that results in a peak Ekman transport divergence there. In our simulations, and as described in GM17, an ITCZ shift results in a pattern of wind stress anomalies that are linear about the equator and, when those anomalies are divided by the Coriolis parameter, Ekman transport anomalies which are roughly constant with latitude and do not affect the surface divergence at the equator. Thus, ITCZ shifts do not result in changes in the upwelling. This result agrees with Miyama et al. (2003), which describes the cross-equatorial cell in the Indian Ocean as driven by surface zonal wind stresses that are similarly linear and asymmetric about the equator. Should the STCs' upwelling zone be coupled to the ITCZ position and shift off of the equator, the water in the lower limb of one hemisphere's STC would have to reverse the sign of its potential vorticity to cross the equator. It could cross the equator in a western boundary current, like the CEC's lower branch in our simulations, or by mixing with water from the other hemisphere (e.g. Hüttl-Kabus and Böning 2008). Above, an atmospheric streamfunction that would be consistent with off-equatorial upwelling would be relatively vertically uniform, with values at the top of the Ekman layer very similar to those near the tropopause and vertical velocities that are constant with pressure. This is not the case for either our polar-amplified forcing simulations (Fig. 5a) or tropics-only forcing simulations (Fig. 12a), which both have atmospheric streamfunctions with meridional mass transports that are weaker near the surface than they are near the tropopause and vertical velocities that peak at about 500 hPa. This decoupling of the Ekman mass transport from the total Hadley cell mass transport has important implications for the CEC's energy transport.

The second point where our results differ from the framework proposed by Schneider (2017) is the strength of the CEC. Schneider assumes that the wind-driven CEC has the same strength as the cross-equatorial Hadley cell; in our simulations, the CECs are much weaker than their atmospheric

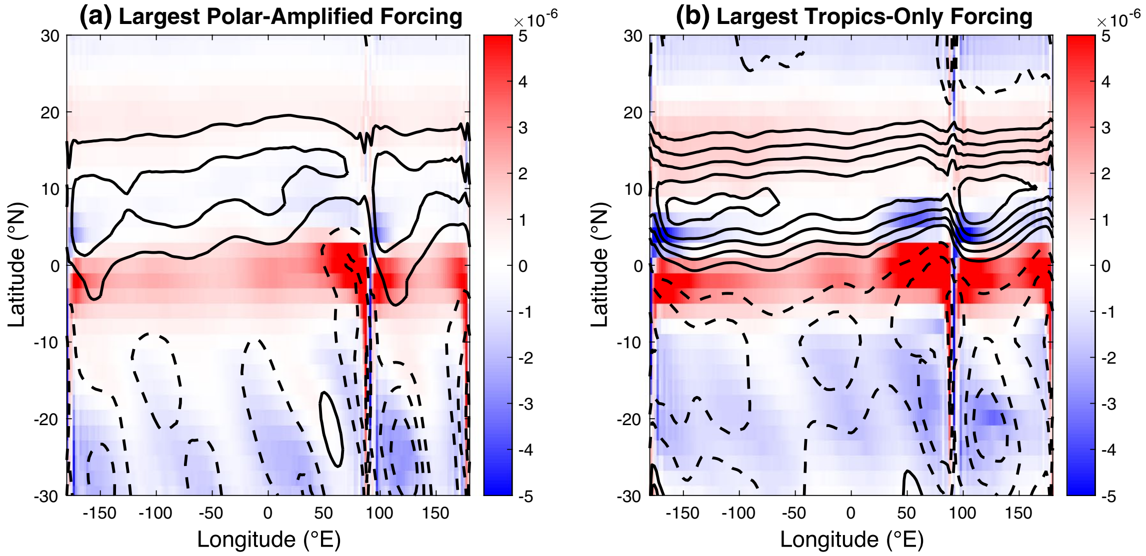

Fig. 14 Vertical motion in the atmosphere and ocean in the fully coupled model for the highest amplitude **a** polar-amplified and **b** tropics-only forcing cases. Colors indicate annual mean vertical velocity (m s^{-1}) at 55 m depth in the ocean. Contours indicate vertical mean, annual mean pressure velocity in the atmosphere, with negative values and ascent shown as solid contours, and positive values and descent shown as dashed contours. The contour interval is 0.01 Pa s^{-1}, and the zero contour is not shown

counterparts (Fig. 7a). They are broadly in Ekman balance with the surface zonal wind stress, but the Ekman transport is not constrained to be the same strength as the Hadley cells' total mass transport, instead balancing the divergence of angular momentum transport in the tropics as described in Sect. 3.2. This can also be more easily appreciated by examining the vertical structure of the atmospheric mass transport streamfunction (e.g. Fig. 8a): the streamfunction maximum occurs in the mid-troposphere, away from the frictional boundary layer and its associated Ekman transport.

The differences in the two descriptions of the CEC and its heat transport have an impact on how the atmosphere's energy balance is evaluated to predict the magnitude of the ITCZ shift. Schneider (2017) estimates F_O/F_A to be equal to the ratio of the ocean's heat uptake at the equator to the net heating of the atmosphere at the equator, consistent with his assumption that the upwelling zone shifts with the ITCZ. For a northward ITCZ shift, this amounts to an identical shift northward of the vertically and zonally integrated distribution of northward ocean heat transport in the tropics. In our simulations, the effect of the CEC is not to shift the OHT distribution north, but to subtract a relatively constant value throughout the tropics (green line, Fig. 9b). Interestingly, the two approaches to the energy balance give similar estimates for the amplitude of the damping of ITCZ shifts by the ocean circulation, due to offsetting differences in their description of the ocean's cross equatorial heat transport. We describe a CEC that is weaker than the one proposed by Schneider, compensated for by an increase in its gross stability owing to its cooler subsurface branch. We propose that a more physically consistent way to estimate the value of F_O/F_A, and its damping of ITCZ shifts, would be to separately estimate the cross-equatorial mass transports and gross stabilities of the atmosphere and ocean.

6 Summary

For a range of forcing amplitudes and distributions designed to shift the ITCZ in an aquaplanet GCM, we find that shifts are always damped in a model configuration that includes an active ocean circulation relative to a configuration where it is passive, "sticking" the ITCZ to latitudes near the equator. The magnitude of the damping has a weak dependence on the forcing amplitude, decreasing as the amplitude increases, and is strongly affected by the forcing distribution, decreasing when the forcing is confined to the tropics. The reason the ITCZ shifts in the active ocean circulation cases are damped can be diagnosed from the hemispheric energy balance, with the largest contribution coming from the ocean's anomalous cross-equatorial heat transport. This heat transport acts to reduce the interhemispheric heating contrast imposed on the atmosphere and reduces the fraction of the original forcing it must compensate by transporting energy across the equator.

A robust feature of the anomalous ocean circulation is a cross-equatorial cell confined to the thermocline, coupled to the Hadley cells above by the surface zonal wind stress. These CECs have the same features in GM17: for a northward ITCZ shift, warm water transported southward across the equator is pumped into the thermocline at cooler temperatures in the southern hemisphere, returning northward across the equator in a western boundary current. The resulting cross-equatorial energy transport is southward, opposing the original heating of the northern hemisphere relative to the southern. Independent of the details of the subsurface ocean circulation, the energy transported across the equator by the CEC can be estimated from its surface properties, with its strength set by the surface zonal wind stress distribution and its gross stability set by the meridional SST gradient.

Secondary impacts on the ITCZ position by the CEC arise from the distribution of its energy transport. If the distribution of the interhemispheric heating contrast is concentrated at higher latitudes, its mismatch with the CEC's heat transport convergence distribution shifts the atmosphere's "net heating" profile further poleward. Combined with radiative feedbacks that are more negative poleward of 30°, the atmosphere more efficiently radiates the net heating away to space, also damping the ITCZ shift. One limitation of our model is its neglect of the effects of clouds on radiation, whose distribution is highly spatially variable and could impact the radiative response of the atmosphere. Our results, however, point to a potentially limited role for cloud radiative feedbacks: if the ocean is efficient at damping ITCZ shifts, the uncertainty in the ITCZ position due to the uncertainties in cloud radiative feedbacks might actually be quite small. For example, Kay et al. (2016) found that the ITCZ position in a comprehensive GCM was relatively insensitive to the optical properties of SH clouds. Moreover, radiative feedbacks in simulations of global warming using comprehensive GCMs that include clouds are, like in our model, relatively positive equatorward of 30° latitude (Zelinka and Hartmann 2012), and their interaction with the CEC's heat transport would likely also contribute to the damping of ITCZ shifts on Earth.

The CEC can also alter the relationship between the ITCZ position and the atmosphere's cross-equatorial energy transport, but the mechanism by which it does this depends on the metric used to define the ITCZ position. Using a centroid metric based on area-weighting the zonal mean tropical rainfall distribution, we find a reduction in subtropical precipitation in the fully coupled model runs relative to the slab ocean runs. If the energy flux equator is used to locate the ITCZ, the structure of the surface branch of the CEC always results in an anomalous heating of the atmosphere between the equator and the ITCZ, reducing the amount it shifts for a given atmospheric cross-equatorial energy transport anomaly. Both metrics predict a damping of the ITCZ shift in our model.

A strong control on the efficacy of the CEC and its cross-equatorial heat transport is the distribution of the interhemispheric heating contrast. For polar-amplified distributions, the gross stability of the CEC is set by the SST difference between the equator and the latitude of the surface westerly jet in the cooled hemisphere. If the heating distribution is confined to the tropics, the CEC is narrowed and its gross stability is reduced by 20–37% depending on the forcing amplitude. In the case of tropics-only forcing, the narrower CEC aligns with the anomalous Hadley cell, which responds directly to the heating distribution.

For polar-amplified forcing distributions, the CEC is considerably wider than the bulk of the atmospheric streamfunction anomalies—compare Figs. 5c, 6, 7 and 8a—and result in a CEC whose width is set by extratropical dynamics. In all of our experiments, and those of GM17, a polar-amplified heating contrast results in a southward shift of the SH surface westerly jet, and for all but the highest forcing amplitude case here, the NH jet is shifted to the south as well. Year-to-year shifts in the annual mean position of the tropospheric westerly jet in the fully coupled model's control run are, like the polar-amplified forcing runs, associated with polar-amplified temperature anomalies and are dominant modes of the model's interannual variability (not shown). The extratropical zonal wind anomalies in the polar-amplified forcing runs, extending from the tropopause to the surface, have a similar vertical structure as the model's unforced variability. This would imply that the westerly jet shifts in the forced runs result from the projection of the polar-amplified forcing distribution onto a mode of natural variability in the model (Ring and Plumb 2008).

From the perspective of the atmosphere's energy balance, the coupled atmosphere–ocean system is more efficient at compensating a hemispherically asymmetric albedo distribution than the atmosphere is alone. Even for large interhemispheric albedo contrasts, the climatic equator cannot be shifted more than a few degrees off of the geographic equator when the adjustment of the ocean's heat transport is included. The fraction of the heating asymmetry compensated for by the ocean's CEC depends on the distribution of the heating, but its coupling to the Hadley cells and ITCZ means it always acts to reduce the asymmetry and is of the same magnitude as the atmosphere's cross-equatorial energy transport. It is clear that, to accurately simulate or predict the response of the ITCZ to an interhemispheric heating contrast, the impact of the tropical wind-driven circulation and its heat transport must be taken into account.

Acknowledgements This research was supported by a Grant from the National Oceanic and Atmospheric Administration. We appreciate useful comments on earlier drafts from Tim Cronin, Paul O'Gorman, Gerard Roe, Sarah Kang, and one anonymous reviewer. An earlier version of this article was published as a part of Brian Green's PhD thesis, "Coupling of the Intertropical Convergence Zone and the Hadley Cells to the Ocean's Circulation," © 2018 Massachusetts Institute of Technology.

Compliance with ethical standards

Conflict of interest The authors declare that they have no conflict of interest.

References

Adcroft A, Campin JM, Hill C, Marshall J (2004) Implementation of an atmosphere-ocean general circulation model on the expanded spherical cube. Mon Weather Rev 132:2845–2863. https://doi.org/10.1175/MWR2823.1

Bischoff T, Schneider T (2016) The equatorial energy balance, ITCZ position, and double-ITCZ bifurcations. J Clim 29:2997–3013. https://doi.org/10.1175/JCLI-D-15-0328.1

Byrne MP, O'Gorman PA (2013) Land–ocean warming contrast over a wide range of climates: convective quasi-equilibrium theory and idealized simulations. J Clim 26:4000–4016. https://doi.org/10.1175/JCLI-D-12-00262.1

Czaja A, Marshall J (2006) The partitioning of poleward heat transport between the atmosphere and ocean. J Atmos Sci 63:1498–1511. https://doi.org/10.1175/JAS3695.1

Donohoe A, Marshall J, Ferreira D, McGee D (2013) The relationship between ITCZ location and cross-equatorial atmospheric heat transport: from the seasonal cycle to the last glacial maximum. J Clim 26:3597–3618. https://doi.org/10.1175/JCLI-D-12-00467.1

Ferrari R, Ferreira D (2011) What processes drive the ocean heat transport? Oceanmodel 38:171–186. https://doi.org/10.1016/j.ocemod.2011.02.013

Ferreira D, Marshall J, Campin JM (2010) Localization of deep water formation: role of atmospheric moisture transport and geometrical constraints on ocean circulation. J Clim 23:1456–1476. https://doi.org/10.1175/2009JCLI3197.1

Feulner G, Rahmstorf S, Levermann A, Volkwardt S (2013) On the origin of the surface air temperature difference between the hemispheres in Earth's present-day climate. J Clim 26:7136–7150. https://doi.org/10.1175/JCLI-D-12-00636.1

Frierson DMW (2007) The dynamics of idealized convection schemes and their effect on the zonally averaged tropical circulation. J Atmos Sci 64:1959–1976. https://doi.org/10.1175/JAS3935.1

Green B, Marshall J (2017) Coupling of trade winds with ocean circulation damps ITCZ shifts. J Clim 30:4395–4411. https://doi.org/10.1175/JCLI-D-16-0818.1

Griffies SM et al (2005) Formulation of an ocean model for global climate simulations. Ocean Sci 1:45–79. https://doi.org/10.5194/os-1-45-2005

Hawcroft M, Haywood JM, Collins M, Jones A, Jones AC, Stephens G (2016) Southern Ocean albedo, inter-hemispheric energy transports and the double ITCZ: global impacts of biases in a coupled model. Clim Dyn 1–17. https://doi.org/10.1007/s00382-016-3205-5

Held IM (2001) The partitioning of the poleward energy transport between the tropical ocean and atmosphere. J

Atmos Sci 58:943–948. https://doi.org/10.1175/1520-0469(2001)058%3C0943:TPOTPE%3E2.0.CO;2

Hüttl-Kabus S, Böning CW (2008) Pathways and variability of the off-equatorial undercurrents in the Atlantic Ocean. J Geophys Res 113:C10018. https://doi.org/10.1029/2007JC004700

Jackett DR, McDougall TJ (1995) Minimal adjustment of hydrographic profiles to achieve static stability. J Atmos Ocean Technol 12:381–389. https://doi.org/10.1175/1520-0426(1995)012%3C0381:MAOHPT%3E2.0.CO;2

Kang SM, Held IM, Frierson DMW, Zhao M (2008) The response of the ITCZ to extratropical thermal forcing: idealized slab-ocean experiments with a GCM. J Clim 21:3521–3532. https://doi.org/10.1175/2007JCLI2146.1

Kang SM, Frierson DMW, Held IM (2009) The tropical response to extratropical thermal forcing in an idealized GCM: the importance of radiative feedbacks and convective parametrization. J Atmos Sci 66:2812–2827. https://doi.org/10.1175/2009JAS2924.1

Kang SM, Held IM, Xie S-P (2014) Contrasting the tropical responses to zonally asymmetric extratropical and tropical thermal forcing. Clim Dyn 42:2033–2043. https://doi.org/10.1007/s00382-013-1863-0

Kang SM, Seager R, Frierson DMW, Liu X (2015) Croll revisited: why is the northern hemisphere warmer than the southern hemisphere? Clim Dyn 44:1457–1472. https://doi.org/10.1007/s00382-014-2147-z

Kang SM, Shin Y, Xie S-P (2018a) Extratropical forcing and tropical rainfall distribution: energetics framework and ocean Ekman advection. npj Clim Atmos Sci. https://doi.org/10.1038/s41612-017-0004-6

Kang SM, Shin Y, Codron F (2018b) The partitioning of poleward energy transport response between the atmosphere and Ekman flux to prescribed surface forcing in a simplified GCM. Geosci Lett. https://doi.org/10.1186/s40562-018-0124-9

Kay JE, Wall C, Yettella V, Medeiros B, Hannay C, Caldwell P, Bitz C (2016) Global climate impacts of fixing the southern ocean shortwave radiation bias in the community earth system model (CESM). J Clim 29:4617–4636. https://doi.org/10.1175/JCLI-D-15-0358.1

Lindzen RS, Hou AY (1988) Hadley circulations for zonally averaged heating centered off the equator. J Atmos Sci 45:2416–2427. https://doi.org/10.1175/1520-0469(1988)045%3C2416:HCFZAH%3E2.0.CO;2

Marshall J, Adcroft A, Hill C, Perelman L, Heisey C (1997a) A finite-volume, incompressible Navier Stokes model for studies of the ocean on parallel computers. J Geophys Res Oceans 102:5753–5766. https://doi.org/10.1029/96JC02775

Marshall J, Hill C, Perelman L, Adcroft A (1997b) Hydrostatic, quasi-hydrostatic, and nonhydrostatic ocean modeling. J Geophys Res Oceans 102:5733–5752. https://doi.org/10.1029/96JC02776

Marshall J, Adcroft A, Campin JM, Hill C, White A (2004) Atmosphere-ocean modeling exploiting fluid isomorphisms. Mon Weather Rev 132:2882–2894. https://doi.org/10.1175/MWR2835.1

Marshall J, Donohoe A, Ferreira D, McGee D (2014) The ocean's role in setting the mean position of the Inter-Tropical Convergence Zone. Clim Dyn 42:1967–1979. https://doi.org/10.1007/s00382-013-1767-z

Miyama T, McCreary JP Jr, Jensen TG, Loschnigg J, Godfrey S, Ishida A (2003) Structure and dynamics of the Indian-Ocean cross-equatorial cell. Deep Sea Res II 50:2023–2047. https://doi.org/10.1016/S0967-0645(03)00044-4

Munk WH (1950) On the wind-driven ocean circulation. J Meteorol 7:79–93. https://doi.org/10.1175/1520-0469(1950)007%3C0080:OTWDOC%3E2.0.CO;2

Peixoto JP, Oort AH (1992) Physics of climate. American Institute of Physics, New York

Plumb RA, Hou AY (1992) The response of a zonally symmetric atmosphere to subtropical thermal forcing: threshold behavior. J Atmos Sci 49:1790–1799. https://doi.org/10.1175/1520-0469(1992)049%3C1790:TROAZS%3E2.0.CO;2

Ring MJ, Plumb RA (2008) The response of a simplified GCM to axisymmetric forcings: applicability of the fluctuation-dissipation theorem. J Atmos Sci 65:3880–3898. https://doi.org/10.1175/2008JAS2773.1

Rose BEJ, Armour KC, Battisti DS, Feldl N, Koll DDB (2014) The dependence of transient climate sensitivity and radiative feedbacks on the spatial pattern of ocean heat uptake. Geophys Res Lett 41:1071–1078. https://doi.org/10.1002/2013GL058955

Schneider T (2017) Feedback of atmosphere-ocean coupling on shifts of the intertropical convergence zone. Geophys Res Lett 44:11,644–11,653. https://doi.org/10.1002/2017GL075817

Schneider T, Bischoff T, Haug GH (2014) Migrations and dynamics of the intertropical convergence zone. Nature 513:45–53. https://doi.org/10.1038/nature13636

Seo J, Kang SM, Frierson DMW (2014) Sensitivity of intertropical convergence zone movement to the latitudinal position of thermal forcing. J Clim 27:3035–3042. https://doi.org/10.1175/JCLI-D-13-00691.1

Tomas RA, Deser C, Sun L (2016) The role of ocean heat transport in the global climate response to projected arctic sea ice loss. J Clim 29:6841–6859. https://doi.org/10.1175/JCLI-D-15-0651.1

Zelinka MD, Hartmann DL (2012) Climate feedbacks and their implications for poleward energy flux changes in a warming climate. J Clim 25:608–624. https://doi.org/10.1175/JCLI-D-11-00096.1